ACS APPLIED MATERIALS & INTERFACES

www.acsami.org Research Article

Magneto-optical Kerr Effect in Ferroelectric Antiferromagnetic Two-Dimensional Heterostructures

Ning Ding, Kunihiro Yananose, Carlo Rizza, Feng-Ren Fan, Shuai Dong,* and Alessandro Stroppa*

Cite This: ACS Appl. Mater. Interfaces 2023, 15, 22282−22290 Read Online

ACCESS | Metrics & More | Article Recommendations | Supporting Information

ABSTRACT: We studied the magneto-optical Kerr effect (MOKE) of two-dimensional (2D) heterostructure $CrI_3/In_2Se_3/CrI_3$ using density functional theory calculations and symmetry analysis. The spontaneous polarization in the In_2Se_3 ferroelectric layer and the antiferromagnetic ordering in CrI_3 layers break the mirror and the time-reversal symmetry, thus activating MOKE. We show that the Kerr angle can be reversed by either the polarization or the antiferromagnetic order parameter. Our results suggest that ferroelectric and antiferromagnetic 2D heterostructures could be exploited for ultracompact information storage devices, where the information is encoded by the two ferroelectric or the two time-reversed antiferromagnetic states and the read-out is performed optically by MOKE.

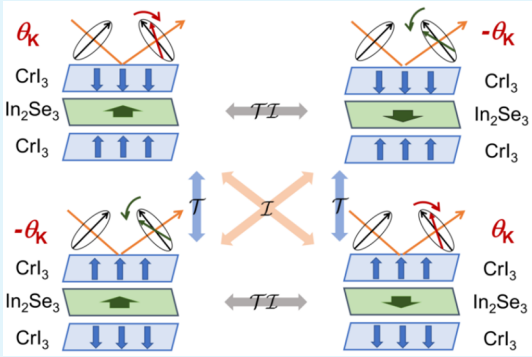

KEYWORDS: *magneto-optical Kerr effect, ferroelectricity, antiferromagnetism, two-dimensional heterostructure, switching behavior, spin texture, two-dimensional magnetism*

Downloaded via SOUTHEAST UNIV on May 10, 2023 at 13:32:12 (UTC).
See https://pubs.acs.org/sharingguidelines for options on how to legitimately share published articles.

■ INTRODUCTION

The magneto-optical Kerr effect (MOKE) characterizes the change of the linear polarization of light reflected from a magnetized surface. It is usually active in ferromagnetic materials, where a spontaneous ferromagnetic ordering breaks the $\mathcal{T}$ (time-reversal) symmetry, leaving a net magnetization in the material. The Kerr rotation is proportional to the sample magnetization, so that MOKE is used to probe ferromagnetism, especially for low-dimensional materials, as a result of its harmlessness to samples and high sensitivity compared to traditional magnetic characterizations, such as elastic neutron scattering.[1−4] MOKE can also be exploited for magneto-optic information storage.[5]

In general, a magnetic material can become magneto-optically active when both the $\mathcal{T}$ and $\mathcal{TI}$ symmetries are broken in the point group,[6,7] where $\mathcal{I}$ is the spatial inversion. This suggests the way to turn on magneto-optical effects by breaking $\mathcal{I}$ symmetry because this automatically breaks $\mathcal{TI}$ symmetry, provided that $\mathcal{T}$ is already broken, like in magnetic systems. Because $\mathcal{I}$ is equivalent to $\mathcal{M}_z\mathcal{C}_2$, where $\mathcal{M}_z$ is the mirror reflection symmetry (mirror perpendicular to the z direction) and $\mathcal{C}_2$ is the in-plane inversion symmetry, the activation of MOKE can be achieved by breaking either $\mathcal{M}_z$ or $\mathcal{C}_2$, as confirmed by some theoretical and experimental reports.[6,8,9] In general, MOKE is not active in antiferromagnetic systems, where the net magnetization is zero and the $\mathcal{TI}$ symmetry is usually preserved. However, several first-principles and experimental studies have predicted or verified a non-negligible MOKE in some antiferromagnets, where the $\mathcal{TI}$ symmetry is broken by either the spatial asymmetry or chirality of the crystal or spin structure even though the net magnetization is zero.[7,8,10−16] In addition to its fundamental interest, the presence of MOKE in an antiferromagnet introduces additional perspectives, because, on the one hand, it challenges the traditional microscopic origin of the Kerr effect, while, on the other hand, it can be exploited in antiferromagnetic spintronics as a result of the insensitivity to external magnetic fields and ultrafast terahertz (THz) spin dynamics.[17−20]

Recently, two-dimensional (2D) materials have been heavily studied because they show interesting physical properties different from bulk systems and can be exploited for miniaturized nanoelectronic components.[21−23] In particular, monolayer CrI_3, one of the first experimentally synthesized low-dimensional magnets, has opened a new era in the study of 2D ferromagnetic materials.[2] Soon after its discovery, many layered magnetic materials have been theoretically predicted and experimentally investigated.[1,24−28] MOKE is a surface-sensitive probe for magnetism, thus naturally attracting

Received: February 24, 2023
Accepted: April 7, 2023
Published: April 20, 2023

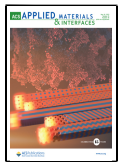

ACS Publications © 2023 American Chemical Society

intensive interest from experimental and theoretical points of view for the study of magnetic 2D systems.[1,2,29−33] Recent studies have shown that MOKE can also be found in 2D antiferromagnetic materials.[6,7,34,35]

Parallel to layered magnets, also, 2D ferroelectric materials, such as In_2Se_3[36] and $CuInP_2S_6$,[37] have received great attention. Inversion symmetry ($\mathcal{I}$) is broken in ferroelectrics by the presence of spontaneous polarization. Therefore, the electric polarization or an external electric field in a layered collinear antiferromagnet may activate MOKE, because the $\mathcal{TI}$ symmetry is also broken, providing the possibility to manipulate MOKE in antiferromagnetic ferroelectrics. For example, Sivadas et al. have recently shown that, for layered collinear antiferromagnets, magneto-optic effects can be generated and manipulated through a gate voltage.[6] This provides a promising route for electric field manipulation of the magneto-optic effects without modifying the underlying magnetic structure in an antiferromagnetic heterostructure (HS). The 2D HSs hold enormous potential for many applications because they can be assembled layer-by-layer to realize or engineer desired physical properties.[38]

In this paper, we investigate a 2D HS composed by an In_2Se_3 ferroelectric monolayer sandwiched between two CrI_3 monolayers with antiferromagnetic coupling, thus forming a ferroelectric antiferromagnetic trilayer, such as $CrI_3/In_2Se_3/CrI_3$ HS. We use density functional theory (DFT) and symmetry analysis for the study of the structural, dynamic, ferroelectric, and magneto-optical properties. Interestingly, the Kerr angle is reversed by the inversion of spontaneous polarization in In_2Se_3 and the spins in CrI_3 monolayers, whereas it vanishes when the spontaneous polarization becomes zero. Furthermore, we investigate how the Kerr switching properties are related to the *k*-space spin textures of the system. Our results suggest the possibility of optically reading the information stored in different polar antiferromagnetic states of the HS using MOKE. Therefore, 2D ferroelectric antiferromagnetic HS may be used for the development of novel and efficient magneto-optical devices in the field of antiferromagnetic spintronics.[39,40]

METHODS

The first-principles calculations based on DFT have been performed using the Vienna *Ab initio* Simulation Package (VASP) code,[41] with the projector augmented wave method implementation in the generalized gradient approximation (GGA) parametrized by Perdew−Burke−Ernzerhof (PBE) for the exchange−correlation functional.[42,43] The Hubbard U_{eff} = 3 eV with the Dudarev parametrization has been applied for properly describing the localization of Cr 3d orbitals.[44] A vacuum layer of 20 Å has been considered to avoid the interaction between the trilayer and the periodic images. The van der Waals (vdW) correction for potential energy with the DFT-D2 method has been used to describe the interlayer interaction among the three monolayers.[45] The Γ-centered *k*-point grid of 9 × 9 × 1 has been employed to sample the Brillouin zone for the static calculation, and the *k*-point grid is enlarged to 11 × 11 × 1 for the dielectric function calculations. We have set the plane-wave cutoff energy to 450 eV. The convergent criterion has been set to 10^{-5} eV for the energy and to 0.01 eV/Å for the Hellman−Feynman forces during the structural optimization.

To evaluate the energy stability, the binding energy (E_b) of the HS was calculated, i.e.

$$E_b = E(\mathrm{HS}) - E(\mathrm{In_2Se_3}) - 2E(\mathrm{CrI_3}) \quad (1)$$

where $E(\mathrm{HS})$, $E(\mathrm{In_2Se_3})$, and $E(\mathrm{CrI_3})$ are the energies of the HS, the In_2Se_3 polar monolayer, and the CrI_3 ferromagnetic monolayer, respectively. The dynamical stability of the trilayer was evaluated on the basis of the phonon spectra, using the finite difference methods.[46−48] The polarization was calculated by the Berry phase method.[49,50]

We have calculated the frequency-dependent relative dielectric tensor ($\underline{\varepsilon}$),[51] which was rescaled as shown in the Methods of the Supporting Information. The relationship between $\underline{\varepsilon}$ and the effective surface optical conductivity tensor $\underline{\underline{\sigma}}$, describing the optical electromagnetic response of the 2D HS,[52] is given by

$$\sigma_{jl} = -id\varepsilon_0\omega[(\varepsilon_{jl} - 1)\delta_{jl} + \varepsilon_{jl}(1 - \delta_{jl})] \quad (2)$$

where $j, l = x, y$, δ_{jl} is the Kronecker delta, d is the trilayer longitudinal thickness, and ε_0 and ω are the vacuum permittivity and the radiation angular frequency, respectively.

STRUCTURES AND SYMMETRIES

Before studying the HS, we considered the individual properties of the isolated monolayers forming the HS. The optimized lattice constants of CrI_3 and In_2Se_3 monolayers are 7.064 and 4.101 Å, respectively. In addition, our calculations show that the CrI_3 and In_2Se_3 monolayers are semiconductors with a direct energy gap of 1.18 eV and an indirect energy band gap of 0.66 eV, respectively. The ferromagnetic moment of CrI_3 is 3 μ_B/Cr, and the polarization of In_2Se_3 is about 2.98 $\mu C/cm^2$ (0.184 eÅ per formula unit) by considering the thickness of the In_2Se_3 monolayer of 6.798 Å along the *z* axis. The results are in good agreement with previous works,[29,36,53,54] thus supporting the accuracy and consistency of our calculations.

To model the HS, a $\sqrt{3} \times \sqrt{3}$ supercell of In_2Se_3 is used to match the unit cell of CrI_3, resulting in a very tiny (0.55%) lattice mismatch. The stacking configuration of the $CrI_3/In_2Se_3/CrI_3$ trilayer with the lowest energy is shown in Figure 1a, where the positions of chromium ions and selenium ions at the top/bottom layer are overlapping along a common vertical axis with AB stacking in the CrI_3 bilayer,[55] as depicted by the dashed lines in Figure 1a.

The space groups of the CrI_3 monolayer and AB-stacking CrI_3 bilayer are $P\bar{3}1m$ (162) and $P\bar{3}$ (147), respectively, where AB stacking indicates that the first layer laterally shifted by [$^2/_3$, $^1/_3$] in fractional coordinates to the second layer.[55] For the In_2Se_3 monolayer, the space groups for ferroelectric and paraelectric states are $P3m1$ (156) and $P\bar{3}m1$ (164), respectively.[36] However, the trilayer HSs with paraelectric and ferroelectric In_2Se_3 have a nonpolar space group $P\bar{3}$ (147) and a polar space group $P3$ (143), respectively.

The easy magnetization axis of the CrI_3 monolayer is perpendicular to the layer plane (i.e., along the *c* axis).[2] Therefore, in the present work, the polar MOKE geometry is considered, where the magnetization axis is along the *z* direction of the trilayer, i.e., perpendicular to the reflection surface and parallel to the plane of incidence. With this direction of the spin moments, the magnetic space groups of the paraelectric trilayer are $P\bar{3}$ [147.13 in the Belov−Neronova−Smirnova (BNS) setting] for the ferromagnetic CrI_3 bilayer and $P\bar{3}'$ (147.15 in the BNS setting) for layered antiferromagnetic CrI_3, which correspond to the magnetic point groups (MPGs) of $\bar{3}$ and $\bar{3}'$, respectively. However, the magnetic space group of the ferroelectric trilayer is $P3$ (143.1 in the BNS setting), regardless of whether the magnetic coupling between the two CrI_3 layers is ferromagnetic or antiferromagnetic.

https://doi.org/10.1021/acsami.3c02680
ACS Appl. Mater. Interfaces 2023, 15, 22282−22290

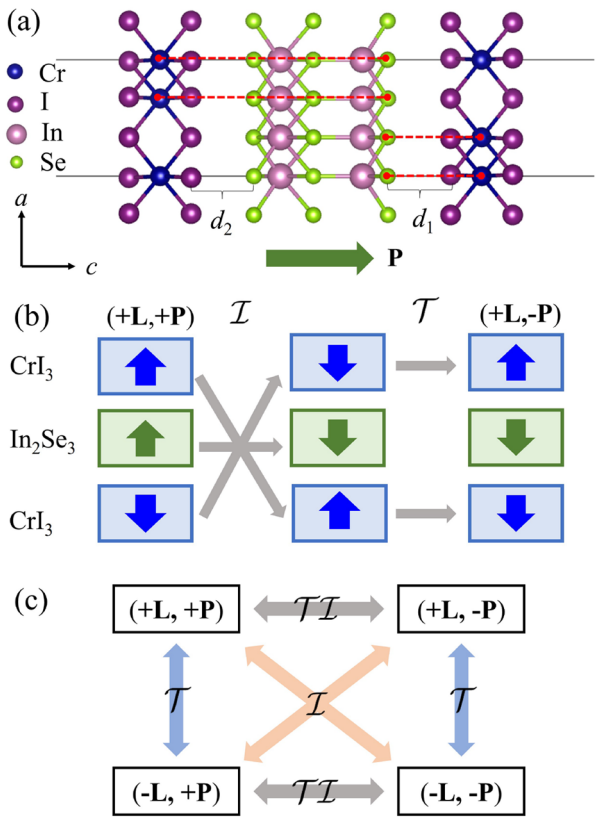

Figure 1. (a) Side view of the ferroelectric−antiferromagnetic trilayer structure, where the green arrow indicates the polarization direction of the In_2Se_3 monolayer. (b) Schematic rule of $\mathcal{I}$ and $\mathcal{T}$ switching in the trilayer, where the blue arrows in CrI_3 denote the spins and the green arrows in In_2Se_3 indicate the ferroelectric polarization. The consequences after each of the $\mathcal{I}$ and $\mathcal{T}$ operations are shown as gray arrows. (c) Symmetry relations of four states. **L**, antiferromagnetic order parameter; **P**, ferroelectric order parameter (i.e., the polarization). The symmetry operations are represented by double-sided arrows.

The traditional approach to evaluate the Kerr rotations from first-principles calculations relies on a well-known formula, which is valid in 3-fold rotational symmetry and suitable for the case where one is not interested in surface-specific phenomena.[56−58] However, the finite thickness in 2D materials limits the application of this approach. Therefore, we provide an extension to take into account the finite thickness of the HS. We consider a monochromatic plane wave normally impinging on a 2D HS on a dielectric substrate and whose electric field is given by $\mathbf{E} = Re(\mathbf{E}_\omega e^{-i\omega t})$, where $\mathbf{E}_\omega = E_{\omega,x}\hat{\mathbf{e}}_x + E_{\omega,y}\hat{\mathbf{e}}_y$. Considering that the HS lies on the plane $z = 0$ and its longitudinal size is much smaller than the radiation wavelength, the HS electromagnetic response can be effectively described by the optically induced surface current density $\mathbf{K} = \underline{\sigma}\mathbf{E}_\omega$, where $\underline{\sigma}$ is the surface conductivity tensor, i.e., a second-rank tensor.[59] Clearly, the form of $\underline{\sigma}$ strongly depends on symmetry. For a paraelectric trilayer, the MPG is $\bar{3}'$, and thus, the surface optical conductivity tensor $\underline{\sigma}$ is a diagonal tensor, where $\sigma_{xx} = \sigma_{yy}$. However, as a result of the MPG of the ferroelectric trilayer (3), $\underline{\sigma}$ can be written as[60,61]

$$\underline{\sigma} = \begin{pmatrix} \sigma_{xx} & \sigma_{xy} \\ -\sigma_{xy} & \sigma_{xx} \end{pmatrix} \tag{3}$$

Next, one can obtain the rigorous reflection coefficients by solving Maxwell's equations and requiring that the electric and magnetic (**H**) fields fulfill the boundary conditions in the presence of the surface current **K**, namely

$$\begin{aligned} &(\mathbf{E}_\omega^> - \mathbf{E}_\omega^<) = 0 \\ &\hat{\mathbf{e}}_z \times (\mathbf{H}_\omega^> - \mathbf{H}_\omega^<) = \mathbf{K} \end{aligned} \tag{4}$$

where > and < indicate the upper ($z > 0$) and lower ($z < 0$) sides of the 2D HS, respectively. The reflection matrix connecting the component of the incident $[\mathbf{E}_\omega^{(i)}]$ and reflected $[\mathbf{E}_\omega^{(r)}]$ electric fields is

$$\begin{pmatrix} E_{\omega,x}^{(r)} \\ E_{\omega,y}^{(r)} \end{pmatrix} = \begin{pmatrix} r_{xx} & r_{xy} \\ r_{yx} & r_{yy} \end{pmatrix} \begin{pmatrix} E_{\omega,x}^{(i)} \\ E_{\omega,y}^{(i)} \end{pmatrix} \tag{5}$$

where

$$\begin{aligned} r_{yy} = r_{xx} &= \frac{1 - (\xi_{xx} + n_s)^2 - \xi_{xy}^{\ 2}}{(n_s + 1 + \xi_{xx})^2 + \xi_{xy}^{\ 2}} \\ r_{xy} = -r_{yx} &= \frac{2\xi_{xy}}{(n_s + 1 + \xi_{xx})^2 + \xi_{xy}^{\ 2}} \end{aligned} \tag{6}$$

is the dimensionless optical conductivity $\xi_{ij} = \sigma_{ij}Z_0$ (Z_0 is the vacuum impedance) and n_s is the substrate refractive index. The complex Kerr angle ϕ can be defined as $\phi_K = r_{xy}/r_{xx} = \theta_K + i\eta_K$ in terms of the rotation angle θ_K and ellipticity η_K,[62] so that

$$\theta_K + i\eta_K = \frac{2\xi_{xy}}{1 - (\xi_{xx} + n_s)^2 - \xi_{xy}^{\ 2}} \tag{7}$$

From eq 7, it is evident that MOKE is activated for $\xi_{xy} \neq 0$.[7] Before calculating the Kerr angle of HS, we confirmed that the CrI_3 monolayer was comparable to the experimental monolayer, as depicted in Figure S1 of the Supporting Information, which can support the accuracy of the following calculation.

Here, we focus our attention on the antiferromagnetic configuration and how the MOKE activity is induced by the electric polarization of the In_2Se_3 monolayer. To describe the system response, we introduce two-order parameters, i.e., $\mathbf{L} = \mathbf{M}_1 - \mathbf{M}_2$ (the antiferromagnetic order parameter) and **P** (ferroelectric order parameter), where the labels 1 and 2 correspond to the bottom and top layers of the CrI_3 bilayer, respectively. Here, **M** and **P** are the spin magnetic moment and electric polarization collinear to the c axis, which is oriented from the bottom to top layer. One can focus on four different states of ferroelectric trilayer antiferromagnets, such as ($+L$, $+P$), ($+L$, $-P$), ($-L$, $+P$), and ($-L$, $-P$), respectively, where $\pm L$ and $\pm P$ are the projections of **L** and **P** along the c axis. These four states can be related by the spatial inversion symmetry ($\mathcal{I}$) and time-reversal symmetry ($\mathcal{T}$), i.e., $\mathcal{I}\mathbf{M} = \mathbf{M}$ and $\mathcal{I}\mathbf{P} = -\mathbf{P}$, while $\mathcal{T}\mathbf{M} = -\mathbf{M}$ and $\mathcal{T}\mathbf{P} = \mathbf{P}$. We summarize the action of the symmetry operations on our system in Figure 1b, and the symmetry relations of the four states are shown in

https://doi.org/10.1021/acsami.3c02680
ACS Appl. Mater. Interfaces 2023, 15, 22282−22290

Figure 1c. For example, $(+L, +P)$ can turn to $(+L, -P)$ by $\mathcal{TI}$ symmetry operation.

RESULTS AND DISCUSSION

The HS shows three stacking modes with 3-fold rotational symmetry. Moreover, the system can have different magnetic orders (see the Supporting Information for further details). Here, we focus on the most energetically favored state reported in Figure 1a. In this case, the lattice constant of the ferroelectric trilayer with antiferromagnetic coupling is $a = b = 6.905$ Å. The optimized interlayer spacings d_1 and d_2 are both 3.218 Å, while the longitudinal thickness (d) is 19.711 Å. The energy of the antiferromagnetic state in the trilayer system is about 0.11 meV/atom higher than that of the ferromagnetic state, i.e., almost degenerate with it. However, the relative energy is very sensitive to computational details, and in addition, it may depend upon the experimental details during the synthesis or preparation of the system. The magneto-optical response and its switching properties are straightforward in the case of ferromagnets; therefore, for the purpose of the present study, we choose to investigate the antiferromagnetic configurations. We calculated the thermodynamic stability by evaluating the binding energy (E_b) of the HS with antiferromagnetic coupling, which is about −44.51 meV/atom. This value is comparable to E_b evaluated in a previous work.[63] For the dynamic stability, we have evaluated the phonon dispersions. As shown in Figure 2a, there is no imaginary frequency within the numerical uncertainty, indicating the dynamic stability of this system.

Although the CrI_3 bilayer is antiferromagnetic (a nearly zero net magnetic moment of $0.001\mu_B$/Cr), the spin-up and spin-down bands are not degenerate as a result of the broken $\mathcal{TI}$ symmetry caused by the existence of polarization, as shown in Figure 2b. The effect is reminiscent of bilayer $MnPSe_3$ gated by an electric field.[6] In our work, the existence of polarization at the $+P$ state induces the conduction band minimum (CBM) of the spin-down (spin-up) channel of the CrI_3 monolayer downward (upward) shift, and this induces the spin-up channel to exhibit a much wider band gap than the spin-down channel, where the spin-up (spin-down) channel corresponds to the bottom (top) CrI_3 layer. Therefore, the band gap reduces, which is a common phenomenon in the vdW HS system.[64−66] The band splitting in the non-centrosymmetric antiferromagnet correlates with the activation of MOKE, which can play the role of exchange splitting. On the other hand, the band structure of the paraelectric trilayer, shown in Figure S3 of the Supporting Information, does not exhibit spin-polarized band splitting, which would correlate with a MOKE inactivity in the paraelectric trilayer system. The band structure with the spin−orbit coupling (SOC) is further split, as reported in Figure 2c.

The easy magnetization axis of the ferroelectric antiferromagnetic trilayer is along the z axis with the magnetic anisotropy energy of 0.56 meV/Cr. The spin configuration of the trilayer is analyzed using FINDSYM, resulting in a MPG 3 as expected.[60,60] Furthermore, according to the MTENSOR tool,[61] the off-diagonal component of dimensionless surface optical conductivity ξ_{xy} should be non-zero in this group, as shown in Figure 3a. Therefore, the Kerr angle of the system has been investigated in the 1.4−6.0 eV photon energy range, which should be more relevant for experiments, as depicted in Figure 3b.

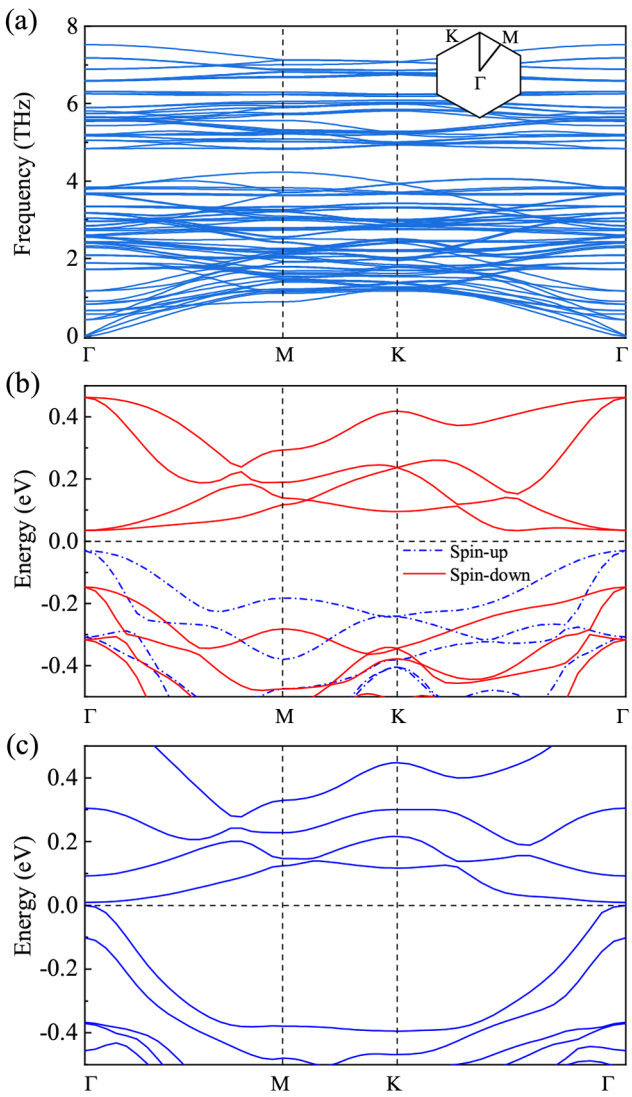

Figure 2. (a) Phonon dispersion curves of ferroelectric trilayer antiferromagnets. The high-symmetry points are defined in the inset. (b and c) Band structures of the ferroelectric trilayer antiferromagnets with the spin polarization but (b) without SOC and (c) with SOC.

Using the transformation rules of the optical conductivity tensor under $\mathcal{I}$ and $\mathcal{T}$ symmetry operations, we note that, under the $\mathcal{I}$ symmetry operation, $\underline{\underline{\sigma}}$ of MPG 3 transforms as follows:

$$\mathcal{I}: \underline{\underline{\sigma}} \rightarrow \mathcal{I}\underline{\underline{\sigma}}\mathcal{I}^{-1} = \underline{\underline{\sigma}} \tag{8}$$

where $\underline{\underline{\sigma}}$ is invariant under inversion operation $\mathcal{I}$. This implies that the Kerr angle is also invariant under inversion in the ferroelectric antiferromagnetic HS.

On the other hand, under the $\mathcal{T}$ symmetry operation, $\underline{\underline{\sigma}}$ of MPG 3 transforms as follows:

$$\mathcal{T}: \underline{\underline{\sigma}} \rightarrow \mathcal{T}\underline{\underline{\sigma}}\mathcal{T}^{-1} = \underline{\underline{\sigma}}^{t} \tag{9}$$

where "t" means the transpose of the conductivity tensor according to Onsager's relation.[67] σ_{xy} as shown in eq 3 changes the sign under $\mathcal{T}$ operation, thus implying that the Kerr angle is also inverted under $\mathcal{T}$ operation according to eq 7. In the same way, it can be shown that the $\mathcal{TI}$ operation can also reverse the Kerr angle in the MPG 3 system.

https://doi.org/10.1021/acsami.3c02680
ACS Appl. Mater. Interfaces 2023, 15, 22282−22290

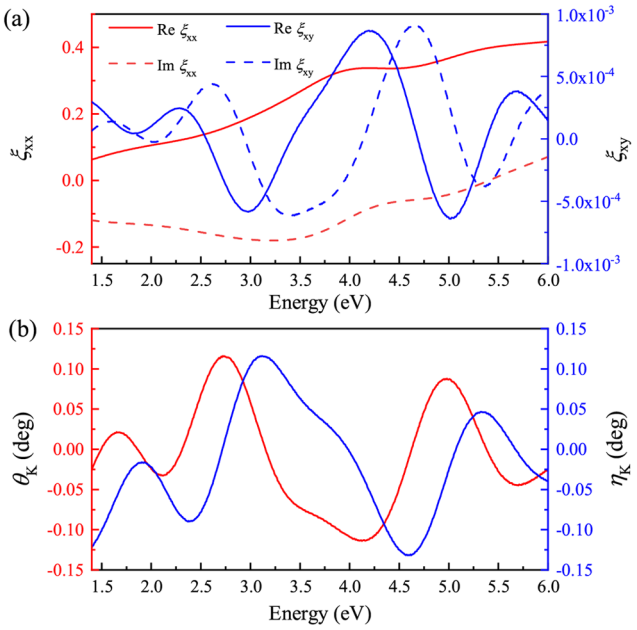

Figure 3. (a) Frequency-dependent dimensionless surface optical conductivity of the $CrI_3/In_2Se_3/CrI_3$ HS in the polar state. (b) Kerr angle θ_K and ellipticity η_K of eq 7 using the dimensionless surface optical conductivity of panel a and setting $n_s = 1$.

It is interesting to investigate the switching rule for the Kerr angle among the four states according to the symmetry relations as depicted in Figure 1c and eq 7, which can be summarized as follows. The Kerr angle can be reversed by either (a) the inversion of polarization **P** or (b) the inversion of antiferromagnetic parameter **L**; in addition, (c) the Kerr angle is invariant, inverting both **P** and **L**. This is summarized in Figure 4a, where we represent the four relevant states on a (P, L) plane, and the switchability (non-switchability) of the Kerr angle is associated with green solid (red dotted) lines. As shown in panels b−d of Figure 4, these predictions based on symmetry are further proven by the first-principles calculations.

Qualitatively, the switching behavior of the Kerr angle can be expressed as follows: $\theta_K(P, L; E) = \alpha PL$, where α is a function of E. Indeed, the sign change of L or P implies the switching of θ_K, but the simultaneous sign change of L and P will not affect θ_K. Furthermore, the formula suggests that different materials, having a different magnitude of P or L, can give different values of the Kerr angle at a specific photon energy. Note that the coefficient α is energy- and material-dependent. To explore this possibility, we perform a series of computational experiments tuning the polarization by artificially shifting the position of the intermediate selenium atoms in the z direction. For the sake of convenience, this artificial displacement (δ) is defined with respect to the atomic positions in the ferroelectric state, as shown in Table 1, thus affecting the final polarization. The results of the Kerr angle with different polarizations are shown in Figure 5. Interestingly, the Kerr angle exhibits a monotonous relation with P at a specific energy value. For example, the Kerr angle at 2.3 eV increases as the polarization increases.

Table 1. Simulated Displacements (δ) Deviating from the Ferroelectric State along the z Direction and the Corresponding Polarization (P)[a]

δ (Å)	−0.08	−0.04	0	0.04	0.08
P (eÅ)	0.459	0.536	0.573	0.610	0.687
P (μC/cm^2)	0.904	1.055	1.128	1.201	1.352

[a]The thickness of HS is d = 19.711 Å.

The physical mechanism can be explained by the different spin splittings with different polarizations, as shown in Figure S6 of the Supporting Information. For example, a larger magnitude of polarization results in a larger downward shift of the CBM of the spin-down channel of the CrI_3 monolayer, and this enlarges the spin splitting; furthermore, it causes a larger Kerr angle and vice versa. These results suggest the possibility

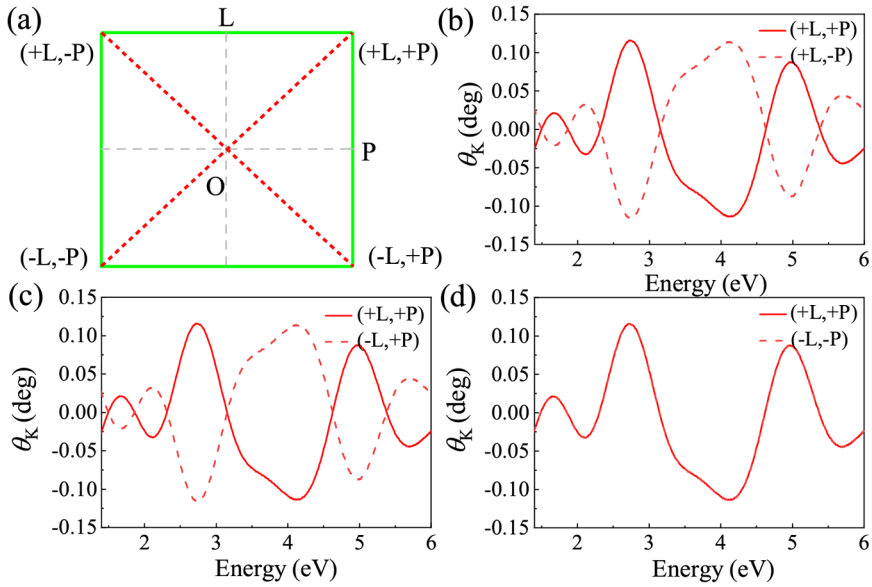

Figure 4. (a) Representation of the dependence of the Kerr angle of the order parameters P and L on a (P, L) plane. The green solid (red dotted) lines represent the switchability (non-switchability) of the Kerr angle. (b−d) Calculated Kerr angle of four states. The solid lines represent ($+L$, $+P$), and the dashed lines represent ($-L$, $+P$), ($-P$, $+L$), and ($-L$, $-P$), respectively.

https://doi.org/10.1021/acsami.3c02680
ACS Appl. Mater. Interfaces 2023, 15, 22282−22290

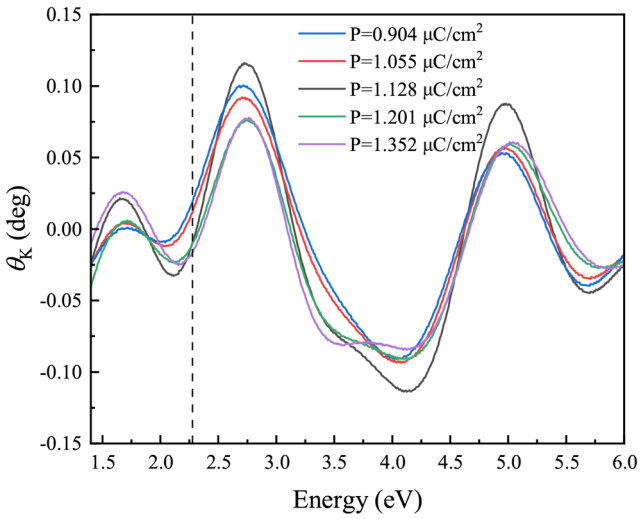

Figure 5. Kerr angle θ_K as a function of the spontaneous polarization P in the considered ferroelectric antiferromagnetic HS (i.e., $CrI_3/In_2Se_3/CrI_3$).

of optimizing the Kerr response for a specific energy range by choosing a suitable ferroelectric and antiferromagnetic composite system.

Finally, we consider how the switching rules discussed for the MOKE response correlate with the spin texture for the highest valence bands in k space for the four different states. We summarize the results in Figure 6. Clearly, the spin texture for the four states has 3-fold rotational symmetry, consistent with the point group C_3, and, accordingly, the spin texture should have a Rashba-type topology.[68] However, the SOC splitting in this work exhibits a different behavior from the conventional Rashba band; there is no linear crossing as a result of the non-existence of Kramers' degeneracy caused by the time-reversal breaking. However, SOC splitting ($\Delta \approx 0.10$ eV) for the highest valence band at the Γ point can be used to indirectly characterize the magnitude of the Rashba parameter, which is compared to that at the Y point ($\Delta \approx 0.09$ eV) of $BiInO_3$.[69] The transformation rules for spin and k by the $\mathcal{I}$, $\mathcal{T}$, and $\mathcal{TI}$ operations are as follows. For $\mathcal{T}$, $(s_x, s_y, s_z) \rightarrow (-s_x, -s_y, -s_z)$ and $(k_x, k_y) \rightarrow (-k_x, -k_y)$. For $\mathcal{I}$, $(s_x, s_y, s_z) \rightarrow (s_x, s_y, s_z)$ and $(k_x, k_y) \rightarrow (-k_x, -k_y)$. In combination of those two effects, for $\mathcal{TI}$, $(s_x, s_y, s_z) \rightarrow (-s_x, -s_y, -s_z)$ and $(k_x, k_y) \rightarrow (k_x, k_y)$. Because the four states are connected by the $\mathcal{T}$, $\mathcal{I}$, or $\mathcal{TI}$ operations, as summarized in Figure 6, it follows that the spin

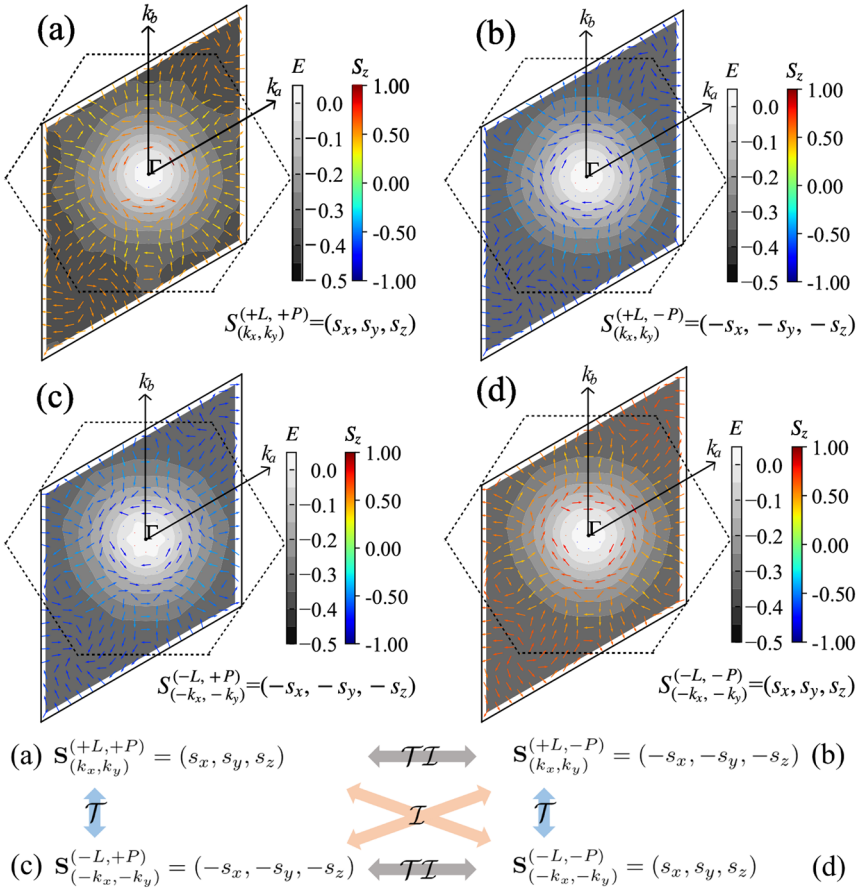

Figure 6. Spin texture, where the in-plane spin components are represented by an arrow and the out-of-plane components are shown in the color map and its relationship of four states for the highest valence band: (a) (+L, +P), (b) (−L, +P), (c) (+L, −P), and (d) (−L, −P). The first Brillouin zone (1st BZ) can be shown by the diamond, which is equivalent to a regular hexagon (the common choice of the 1st BZ of a hexagonal lattice as depicted by the black dotted lines) by shifting its fragments. The energy level with respect to the valence band maximum is illustrated by the gray scale map. The figure at the bottom intuitively describes the relationship between the spin texture and symmetry operations.

https://doi.org/10.1021/acsami.3c02680
ACS Appl. Mater. Interfaces 2023, 15, 22282−22290

texture can be reversed by either P or L reversal, as it happens for the Kerr rotation.

CONCLUSION

We have investigated the 2D ferroelectric antiferromagnetic HS $CrI_3/In_2Se_3/CrI_3$ by focusing on its magneto-optical Kerr effect response. Interestingly, in the antiferromagnetic configuration, MOKE is activated and controlled by the spontaneous electric polarization and the Kerr switching occurs by switching the electric polarization P or the antiferromagnetic order parameter L. Our findings suggest that a 2D HS exhibiting ferroelectricity and antiferromagnetism could provide a novel material platform with potential for information storage in antiferromagnetic spintronics. Finally, a comment is in order. As we discussed, antiferromagnetic materials have drawn considerable attention recently since they are robust against perturbation, produce no stray fields, and exhibit ultrafast dynamics. Understanding how to efficiently manipulate the magnetic state of an antiferromagnet is the key to exploit MOKE in 2D ferroelectric antiferromagnetic HSs. How to manipulate magnetic states of antiferromagnets has been recenlty discussed in Refs 70 and 71.

ASSOCIATED CONTENT

Supporting Information

The Supporting Information is available free of charge at https://pubs.acs.org/doi/10.1021/acsami.3c02680.

More details about the structural information of different stacking modes, electrical properties, and Kerr angle of the B-type $CrI_3/In_2Se_3/CrI_3$ HS (PDF)

AUTHOR INFORMATION

Corresponding Authors

Shuai Dong − *School of Physics, Southeast University, Nanjing, Jiangsu 21189, People's Republic of China;* orcid.org/0000-0002-6910-6319; Email: sdong@seu.edu.cn

Alessandro Stroppa − *Consiglio Nazionale delle Ricerche, Institute for Superconducting and Innovative Materials and Devices (CNR−SPIN) and Department of Physical and Chemical Sciences, University of L'Aquila, I-67100 Coppito, L'Aquila, Italy;* orcid.org/0000-0001-6067-0434; Email: alessandro.stroppa@spin.cnr.it

Authors

Ning Ding − *School of Physics, Southeast University, Nanjing, Jiangsu 21189, People's Republic of China*

Kunihiro Yananose − *Center for Theoretical Physics, Department of Physics and Astronomy, Seoul National University, Seoul 08826, Republic of Korea*

Carlo Rizza − *Department of Physical and Chemical Sciences, University of L'Aquila, I-67100 Coppito, L'Aquila, Italy*

Feng-Ren Fan − *Department of Physics and Guangdong-Hong Kong Joint Laboratory of Quantum Matter, The University of Hong Kong, Hong Kong, People's Republic of China*

Complete contact information is available at: https://pubs.acs.org/10.1021/acsami.3c02680

Notes

The authors declare no competing financial interest.

ACKNOWLEDGMENTS

The authors thank Ke Yang of University of Shanghai for Science and Technology and Xue-Zeng Lu, Haoshen Ye, and Kaidi Xu of Southeast University for fruitful discussions. This work was supported by the National Natural Science Foundation of China (Grants 12274069 and 11834002) and the Postgraduate Research & Practice Innovation Program of Jiangsu Province (Grant KYCX22_0241). The authors acknowledge the Project HPC-EUROPA3 (INFRAIA-2016-1-730897), with the support of the EC Research Innovation Action under the H2020 Programme, in particular, the computer resources and technical support provided by CINECA−HPC and the Big Data Center of Southeast University for providing the facility support on the calculations. Research at SPIN−CNR and University of L'Aquila has been funded by the European Union−NextGenerationEU under the Italian Ministry of University and Research (MUR) National Innovation Ecosystem Grant ECS00000041-VITALITY. Alessandro Stroppa (A. S.) and Carlo Rizza acknowledge Università degli Studi di Perugia, Universitá degli Studi dell'Aquila, and MUR for support within the project Vitality. A. S. acknowledges Prof. Kian Ping Loh (The Hong Kong Polytechnic University) and Franco D'Orazio (University of L'Aquila) for interesting discussions.

REFERENCES

(1) Gong, C.; Li, L.; Li, Z.; Ji, H.; Stern, A.; Xia, Y.; Cao, T.; Bao, W.; Wang, C.; Wang, Y.; Qiu, Z. Q.; Cava, R. J.; Louie, S. G.; Xia, J.; Zhang, X. Discovery of Intrinsic Ferromagnetism in Two-Dimensional van der Waals Crystals. *Nature* **2017**, *546*, 265−269.

(2) Huang, B.; Clark, G.; Navarro-Moratalla, E.; Klein, D. R.; Cheng, R.; Seyler, K. L.; Zhong, D.; Schmidgall, E.; McGuire, M. A.; Cobden, D. H.; Yao, W.; Xiao, D.; Jarillo-Herrero, P.; Xu, X. Layer-Dependent Ferromagnetism in a van der Waals Crystal Down to the Monolayer Limit. *Nature* **2017**, *546*, 270−273.

(3) Ribeiro, M.; Gentile, G.; Marty, A.; Dosenovic, D.; Okuno, H.; Vergnaud, C.; Jacquot, J.-F.; Jalabert, D.; Longo, D.; Ohresser, P.; Hallal, A.; Chshiev, M.; Boulle, O.; Bonell, F.; Jamet, M. Large-Scale Epitaxy of Two-Dimensional van der Waals Room-Temperature Ferromagnet Fe_5GeTe_2. *npj 2D Mater. Appl.* **2022**, *6*, 10.

(4) Maccaferri, N.; Inchausti, X.; García-Martín, A.; Cuevas, J. C.; Tripathy, D.; Adeyeye, A. O.; Vavassori, P. Resonant Enhancement of Magneto-Optical Activity Induced by Surface Plasmon Polariton Modes Coupling in 2D Magnetoplasmonic Crystals. *ACS Photonics* **2015**, *2*, 1769−1779.

(5) Tsunashima, S. Magneto-Optical Recording. *J. Phys. D: Appl. Phys.* **2001**, *34*, R87.

(6) Sivadas, N.; Okamoto, S.; Xiao, D. Gate-Controllable Magneto-Optic Kerr Effect in Layered Collinear Antiferromagnets. *Phys. Rev. Lett.* **2016**, *117*, 267203.

(7) Yang, K.; Hu, W.; Wu, H.; Whangbo, M.-H.; Radaelli, P. G.; Stroppa, A. Magneto-Optical Kerr Switching Properties of $(CrI_3)_2$ and $(CrBr_3/CrI_3)$ Bilayers. *ACS Appl. Electron. Mater.* **2020**, *2*, 1373−1380.

(8) Feng, W.; Guo, G.-Y.; Zhou, J.; Yao, Y.; Niu, Q. Large Magneto-Optical Kerr Effect in Noncollinear Antiferromagnets Mn_3X (X = Rh, Ir, Pt). *Phys. Rev. B* **2015**, *92*, 144426.

(9) Feng, W.; Guo, G.-Y.; Yao, Y. Tunable Magneto-Optical Effects in Hole-Doped Group-IIIA Metal-Monochalcogenide Monolayers. *2D Mater.* **2017**, *4*, 015017.

(10) Yang, X.; Yang, P.; Zhou, X.; Feng, W.; Yao, Y. First-and Second-Order Magneto-Optical Effects and Intrinsically Anomalous Transport in the Two-Dimensional van der Waals Layered Magnets CrXY (X = S, Se, Te; Y = Cl, Br, I). *Phys. Rev. B* **2022**, *106*, 054408.

(11) Feng, W.; Hanke, J.-P.; Zhou, X.; Guo, G.-Y.; Blügel, S.; Mokrousov, Y.; Yao, Y. Topological Magneto-Optical Effects and

Their Quantization in Noncoplanar Antiferromagnets. *Nat. Commun.* **2020**, *11*, 118.
(12) Zhou, X.; Feng, W.; Yang, X.; Guo, G.-Y.; Yao, Y. Crystal Chirality Magneto-Optical Effects in Collinear Antiferromagnets. *Phys. Rev. B* **2021**, *104*, 024401.
(13) Higo, T.; Man, H.; Gopman, D. B.; Wu, L.; Koretsune, T.; van 't Erve, O. M. J.; Kabanov, Y. P.; Rees, D.; Li, Y.; Suzuki, M.-T.; Patankar, S.; Ikhlas, M.; Chien, C. L.; Arita, R.; Shull, R. D.; Orenstein, J.; Nakatsuji, S. Large Magneto-Optical Kerr Effect and Imaging of Magnetic Octupole Domains in an Antiferromagnetic Metal. *Nat. Photonics* **2018**, *12*, 73−78.
(14) Fan, F.-R.; Wu, H.; Nabok, D.; Hu, S.; Ren, W.; Draxl, C.; Stroppa, A. Electric-Magneto-Optical Kerr Effect in a Hybrid Organic−Inorganic Perovskite. *J. Am. Chem. Soc.* **2017**, *139*, 12883−12886.
(15) Wu, M.; Isshiki, H.; Chen, T.; Higo, T.; Nakatsuji, S.; Otani, Y. Magneto-Optical Kerr Effect in a Non-Collinear Antiferromagnet Mn_3Ge. *Appl. Phys. Lett.* **2020**, *116*, 132408.
(16) Uchimura, T.; Yoon, J.-Y.; Sato, Y.; Takeuchi, Y.; Kanai, S.; Takechi, R.; Kishi, K.; Yamane, Y.; DuttaGupta, S.; Ieda, J.; Ohno, H.; Fukami, S. Observation of Domain Structure in Non-Collinear Antiferromagnetic Mn_3Sn Thin Films by Magneto-Optical Kerr Effect. *Appl. Phys. Lett.* **2022**, *120*, 172405.
(17) Jungwirth, T.; Marti, X.; Wadley, P.; Wunderlich, J. Antiferromagnetic Spintronics. *Nat. Nanotechnol.* **2016**, *11*, 231−241.
(18) Rustagi, A.; Bharatbhai Solanki, A.; Tserkovnyak, Y.; Upadhyaya, P. Coupled Spin-Charge Dynamics in Magnetic van der Waals Heterostructures. *Phys. Rev. B* **2020**, *102*, 094421.
(19) Yan, H.; Feng, Z.; Qin, P.; Zhou, X.; Guo, H.; Wang, X.; Chen, H.; Zhang, X.; Wu, H.; Jiang, C.; Liu, Z. Electric-Field-Controlled Antiferromagnetic Spintronic Devices. *Adv. Mater.* **2020**, *32*, 1905603.
(20) Ma, J.; Gu, F.; Xu, Y.; Le, J.; Zeng, F.; Wu, Y.; Tian, C. Improving the Sensitivity of DC Magneto-Optical Kerr Effect Measurement to 10^{-7} rad/Hz. *Chin. Opt. Lett.* **2022**, *20*, 111201.
(21) Burch, K. S.; Mandrus, D.; Park, J.-G. Magnetism in Two-Dimensional van der Waals Materials. *Nature* **2018**, *563*, 47−52.
(22) Gong, C.; Zhang, X. Two-Dimensional Magnetic Crystals and Emergent Heterostructure Devices. *Science* **2019**, *363*, No. eaav4450.
(23) Zhang, D.; Schoenherr, P.; Sharma, P.; Seidel, J. Ferroelectric Order in van der Waals Layered Materials. *Nat. Rev. Mater.* **2023**, *8*, 25−40.
(24) Deng, Y.; Yu, Y.; Song, Y.; Zhang, J.; Wang, N. Z.; Sun, Z.; Yi, Y.; Wu, Y. Z.; Wu, S.; Zhu, J.; Wang, J.; Chen, X. H.; Zhang, Y. Gate-Tunable Room-Temperature Ferromagnetism in Two-Dimensional Fe_3GeTe_2. *Nature* **2018**, *563*, 94−99.
(25) Ding, N.; Chen, J.; Dong, S.; Stroppa, A. Ferroelectricity and Ferromagnetism in a VOI_2 Monolayer: Role of the Dzyaloshinskii-Moriya Interaction. *Phys. Rev. B* **2020**, *102*, 165129.
(26) An, M.; Dong, S. Ferroic Orders in Two-Dimensional Transition/Rare-Earth Metal Halides. *APL Mater.* **2020**, *8*, 110704.
(27) You, H.; Ding, N.; Chen, J.; Yao, X.; Dong, S. Gadolinium Halide Monolayers: A Fertile Family of Two-Dimensional 4f Magnets. *ACS Appl. Electron. Mater.* **2022**, *4*, 3168−3176.
(28) Chu, J.; Wang, Y.; Wang, X.; Hu, K.; Rao, G.; Gong, C.; Wu, C.; Hong, H.; Wang, X.; Liu, K.; Gao, C.; Xiong, J. 2D Polarized Materials: Ferromagnetic, Ferrovalley, Ferroelectric Materials, and Related Heterostructures. *Adv. Mater.* **2021**, *33*, 2004469.
(29) Wu, M.; Li, Z.; Cao, T.; Louie, S. G. Physical Origin of Giant Excitonic and Magneto-Optical Responses in Two-Dimensional Ferromagnetic Insulators. *Nat. Commun.* **2019**, *10*, 2371.
(30) Jiang, M.-C.; Guo, G.-Y. Large Magneto-Optical Effect and Magnetic Anisotropy Energy in Two-Dimensional Metallic Ferromagnet Fe_3GeTe_2. *Phys. Rev. B* **2022**, *105*, 014437.
(31) Gudelli, V. K.; Guo, G.-Y. Magnetism and Magneto-Optical Effects in Bulk and Few-Layer CrI_3: A Theoretical GGA+*U* Study. *New J. Phys.* **2019**, *21*, 053012.
(32) Fang, Y.; Wu, S.; Zhu, Z.-Z.; Guo, G.-Y. Large Magneto-Optical Effects and Magnetic Anisotropy Energy in Two-Dimensional $Cr_2Ge_2Te_6$. *Phys. Rev. B* **2018**, *98*, 125416.
(33) Molina-Sánchez, A.; Catarina, G.; Sangalli, D.; Fernández-Rossier, J. Magneto-Optical Response of Chromium Trihalide Monolayers: Chemical Trends. *J. Mater. Chem. C* **2020**, *8*, 8856−8863.
(34) Yananose, K.; Radaelli, P. G.; Cuoco, M.; Yu, J.; Stroppa, A. Activating Magnetoelectric Optical Properties by Twisting Antiferromagnetic Bilayers. *Phys. Rev. B* **2022**, *106*, 184408.
(35) Wang, N.; Chen, J.; Ding, N.; Zhang, H.; Dong, S.; Wang, S.-S. Magneto-Optical Kerr Effect and Magnetoelasticity in a Weakly Ferromagnetic RuF_4 Monolayer. *Phys. Rev. B* **2022**, *106*, 064435.
(36) Ding, W.; Zhu, J.; Wang, Z.; Gao, Y.; Xiao, D.; Gu, Y.; Zhang, Z.; Zhu, W. Prediction of Intrinsic Two-Dimensional Ferroelectrics in In_2Se_3 and Other III_2-V_3 van der Waals Materials. *Nat. Commun.* **2017**, *8*, 14956.
(37) Liu, F.; You, L.; Seyler, K. L.; Li, X.; Yu, P.; Lin, J.; Wang, X.; Zhou, J.; Wang, H.; He, H.; Pantelides, S. T.; Zhou, W.; Sharma, P.; Xu, X.; Ajayan, P. M.; Wang, J.; Liu, Z. Room-Temperature Ferroelectricity in $CuInP_2S_6$ Ultrathin Flakes. *Nat. Commun.* **2016**, *7*, 12357.
(38) Geim, A. K.; Grigorieva, I. V. Van der Waals Heterostructures. *Nature* **2013**, *499*, 419−425.
(39) Wadley, P.; Howells, B.; Železný, J.; Andrews, C.; Hills, V.; Campion, R. P.; Novák, V.; Olejník, K.; Maccherozzi, F.; Dhesi, S. S.; Martin, S. Y.; Wagner, T.; Wunderlich, J.; Freimuth, F.; Mokrousov, Y.; Kuneš, J.; Chauhan, J. S.; Grzybowski, M. J.; Rushforth, A. W.; Edmonds, K. W.; Gallagher, B. L.; Jungwirth, T. Electrical Switching of an Antiferromagnet. *Science* **2016**, *351*, 587−590.
(40) Winter, L.; Großenbach, S.; Nowak, U.; Rózsa, L. Nutational Switching in Ferromagnets and Antiferromagnets. *Phys. Rev. B* **2022**, *106*, 214403.
(41) Kresse, G.; Furthmüller, J. Efficient Iterative Schemes for *ab initio* Total-Energy Calculations Using a Plane-Wave Basis Set. *Phys. Rev. B* **1996**, *54*, 11169−11186.
(42) Kresse, G.; Joubert, D. From Ultrasoft Pseudopotentials to the Projector Augmented-Wave Method. *Phys. Rev. B* **1999**, *59*, 1758−1775.
(43) Perdew, J. P.; Burke, K.; Ernzerhof, M. Generalized Gradient Approximation Made Simple. *Phys. Rev. Lett.* **1996**, *77*, 3865−3868.
(44) Dudarev, S. L.; Botton, G. A.; Savrasov, S. Y.; Humphreys, C. J.; Sutton, A. P. Electron-Energy-Loss Spectra and the Structural Stability of Nickel Oxide: An LSDA+*U* study. *Phys. Rev. B* **1998**, *57*, 1505−1509.
(45) Grimme, S. Semiempirical GGA-Type Density Functional Constructed with a Long-Range Dispersion Correction. *J. Comput. Chem.* **2006**, *27*, 1787−1799.
(46) Togo, A.; Tanaka, I. First Principles Phonon Calculations in Materials Science. *Scr. Mater.* **2015**, *108*, 1−5.
(47) Le Page, Y.; Saxe, P. Symmetry-General Least-Squares Extraction of Elastic Data for Strained Materials from *ab initio* Calculations of Stress. *Phys. Rev. B* **2002**, *65*, 104104.
(48) Wu, X.; Vanderbilt, D.; Hamann, D. R. Systematic Treatment of Displacements, Strains, and Electric Fields in Density-Functional Perturbation Theory. *Phys. Rev. B* **2005**, *72*, 035105.
(49) Resta, R. Macroscopic Polarization in Crystalline Dielectrics: The Geometric Phase Approach. *Rev. Mod. Phys.* **1994**, *66*, 899−915.
(50) King-Smith, R. D.; Vanderbilt, D. Theory of Polarization of Crystalline Solids. *Phys. Rev. B* **1993**, *47*, 1651−1654.
(51) Gajdoš, M.; Hummer, K.; Kresse, G.; Furthmüller, J.; Bechstedt, F. Linear Optical Properties in the Projector-Augmented Wave Methodology. *Phys. Rev. B* **2006**, *73*, 045112.
(52) Othman, M. A.; Guclu, C.; Capolino, F. Graphene-Based Tunable Hyperbolic Metamaterials and Enhanced Near-Field Absorption. *Opt. Express* **2013**, *21*, 7614−7632.
(53) McGuire, M. A.; Dixit, H.; Cooper, V. R.; Sales, B. C. Coupling of Crystal Structure and Magnetism in the Layered, Ferromagnetic Insulator CrI_3. *Chem. Mater.* **2015**, *27*, 612−620.
(54) Li, C.; Li, Y.; Tang, Y.; Zheng, S.; Zhang, J.; Zhang, Y.; Lin, L.; Yan, Z.; Jiang, X.; Liu, J.-M. Band Structure, Ferroelectric Instability,

https://doi.org/10.1021/acsami.3c02680
ACS Appl. Mater. Interfaces 2023, 15, 22282−22290

and Spin−Orbital Coupling Effect of Bilayer α-In_2Se_3. *J. Appl. Phys.* **2020**, *128*, 234106.
(55) Sivadas, N.; Okamoto, S.; Xu, X.; Fennie, C. J.; Xiao, D. Stacking-Dependent Magnetism in Bilayer CrI_3. *Nano Lett.* **2018**, *18*, 7658−7664.
(56) Ebert, H. Magneto-Optical Effects in Transition Metal Systems. *Rep. Prog. Phys.* **1996**, *59*, 1665.
(57) Sangalli, D.; Marini, A.; Debernardi, A. Pseudopotential-Based First-Principles Approach to the Magneto-Optical Kerr Effect: From Metals to the Inclusion of Local Fields and Excitonic Effects. *Phys. Rev. B* **2012**, *86*, 125139.
(58) Rosa, P.; Sangalli, D.; Onida, G.; Debernardi, A. *Ab initio* Electronic Structure, Optical, and Magneto-Optical Properties of MnGaAs Digital Ferromagnetic Heterostructures. *Phys. Rev. B* **2015**, *91*, 075207.
(59) Yoshino, T. Theory for Oblique-Incidence Magneto-Optical Faraday and Kerr Effects in Interfaced Monolayer Graphene and Their Characteristic Features. *J. Opt. Soc. Am.* **2013**, *30*, 1085−1091.
(60) Stokes, H. T.; Hatch, D. M. FINDSYM: Program for Identifying the Space-Group Symmetry of a Crystal. *J. Appl. Crystallogr.* **2005**, *38*, 237−238.
(61) Gallego, S. V.; Etxebarria, J.; Elcoro, L.; Tasci, E. S.; Perez-Mato, J. M. Automatic Calculation of Symmetry-Adapted Tensors in Magnetic and Non-Magnetic Materials: A New Tool of the Bilbao Crystallographic Server. *Acta Crystallogr. A* **2019**, *75*, 438−447.
(62) Ricci, F.; D'Orazio, F.; Continenza, A.; Lucari, F.; Freeman, A. J. First-Principles Modeling of the Magneto-Optical Response in Inhomogeneous Systems. *Phys. Rev. B* **2008**, *78*, 134411.
(63) Liu, X.; Shen, C.; Li, X.; Wang, T.; He, M.; Li, L.; Wang, Y.; Li, J.; Xia, C. Magnetoelectric Coupling Effects on the Band Alignments of Multiferroic In_2Se_3-CrI_3 Trilayer Heterostructures. *Nanoscale* **2022**, *14*, 5454−5461.
(64) Chen, Y.; Wang, X.; Huang, L.; Wang, X.; Jiang, W.; Wang, Z.; Wang, P.; Wu, B.; Lin, T.; Shen, H.; Wei, Z.; Hu, W.; Meng, X.; Chu, J.; Wang, J. Ferroelectric-Tuned van der Waals Heterojunction with Band Alignment Evolution. *Nat. Commun.* **2021**, *12*, 4030.
(65) Qiu, Z.; Trushin, M.; Fang, H.; Verzhbitskiy, I.; Gao, S.; Laksono, E.; Yang, M.; Lyu, P.; Li, J.; Su, J.; Telychko, M.; Watanabe, K.; Taniguchi, T.; Wu, J.; Neto, A. H. C.; Yang, L.; Eda, G.; Adam, S.; Lu, J. Giant Gate-Tunable Bandgap Renormalization and Excitonic Effects in a 2D Semiconductor. *Sci. Adv.* **2019**, *5*, No. eaaw2347.
(66) Zhang, C.; Huang, H.; Ni, X.; Zhou, Y.; Kang, L.; Jiang, W.; Chen, H.; Zhong, J.; Liu, F. Band Gap Reduction in van der Waals Layered 2D Materials via a De-Charge Transfer Mechanism. *Nanoscale* **2018**, *10*, 16759−16764.
(67) Rathgen, H.; Katsnelson, M. I.; Eriksson, O.; Zwicknagl, G. Polar Magneto-Optical Kerr Effect for Low-Symmetric Ferromagnets. *Phys. Rev. B* **2005**, *72*, 014451.
(68) Tao, L. L.; Tsymbal, E. Y. Perspectives of Spin-Textured Ferroelectrics. *J. Phys. D: Appl. Phys.* **2021**, *54*, 113001.
(69) Tao, L.; Tsymbal, E. Y. Persistent Spin Texture Enforced by Symmetry. *Nat. Commun.* **2018**, *9*, 2763.
(70) Song, C.; You, Y.; Chen, X.; Zhou, X.; Wang, Y.; Pan, F. How to Manipulate Magnetic States of Antiferromagnets. *Nanotechnology* **2018**, *29*, 112001.
(71) Baltz, V.; Manchon, A.; Tsoi, M.; Moriyama, T.; Ono, T.; Tserkovnyak, Y. Antiferro-magnetic Spintronics. *Rev. Mod. Phys.* **2018**, *90*, 015005.

■ NOTE ADDED AFTER ASAP PUBLICATION

Due to a production error, this paper was published ASAP on April 20, 2023, with two missing references and the wrong version of the Supporting Information. The corrected version reposted on April 21, 2023.

https://doi.org/10.1021/acsami.3c02680
ACS Appl. Mater. Interfaces 2023, 15, 22282−22290